doi:10.20944/preprints202004.0055.v1

Automatic quality assessments of laser powder bed fusion builds from photodiode sensor measurements

Sarini Jayasinghe[a], Paolo Paoletti[a,b], Chris Sutcliffe[a], John Dardis[c], Nick Jones[c], Peter L. Green[a,b]

[a] *School of Engineering, University of Liverpool,Harrison Hughes Building,Liverpool,L69 3GH,United Kingdom*
[b] *Institute for Risk and Uncertainty, University of Liverpool, Chadwick Building, Peach Street, Liverpool L69 7ZF, United Kingdom*
[c] *Renishaw Plc, New Mills, Kingswood, Wotton-under-Edge GL12 8JR, United Kingdom*

Abstract

This study evaluates whether a combination of photodiode sensor measurements, taken during laser powder bed fusion (L-PBF) builds, can be used to predict the resulting build quality via a purely data-based approach. We analyse the relationship between build density and features that are extracted from sensor data collected from three different photodiodes. The study uses a Singular Value Decomposition to extract lower-dimensional features from photodiode measurements, which are then fed into machine learning algorithms. Several unsupervised learning methods are then employed to classify low density ($<$ 99% part density) and high density ($\geq$ 99% part density) specimens. Subsequently, a supervised learning method (Gaussian Process regression) is used to directly predict build density. Using the unsupervised clustering approaches, applied to features extracted from both photodiode sensor data as well as observations relating to the energy transferred to the material, build density was predicted with up to 93.54% accuracy. With regard to the supervised regression approach, a Gaussian Process algorithm was capable of predicting the build density with a RMS error of 3.65%. The study shows, therefore, that there is potential for machine learning algorithms to predict indicators of L-PBF build quality from photodiode build-measurements. Moreover, the work herein describes approaches that are predominantly probabilistic, thus facilitating uncertainty quantification in machine-learnt predictions of L-PBF build quality.

---

[*] Corresponding author
Email address: `plgreen@liverpool.ac.uk` (Peter L. Green)

Preprint submitted to Additive Manufacturing *April 4, 2020*

doi:10.20944/preprints202004.0055.v1

Keywords: Laser powder bed fusion, automatic quality assessment, machine learning, automatic relevance determination.

---

1. Introduction

The potential for Additive Manufacturing (AM) to lead to a reduction in production steps and higher resource efficiency have encouraged the adoption of AM for serial production over conventional manufacturing processes such as milling, grinding, drilling, boring etc. Consequently, over a span of two decades, AM has become a multi-billion dollar industry [1]. The 2017 UK industrial strategy white paper [2] states that businesses have begun to exploit the potential of AM to make transformational improvements to productivity. Although the most widely used application of AM technologies so far has been rapid prototyping [1], the cost-effectiveness of the process and the ability of AM to fabricate geometrically complex and light-weight parts has increased the demand for AM end-use products. These include, for example, applications in aerospace and bio-medical industries. In order to meet the certification constraints imposed by these sectors, ensuring the quality of AM-produced parts is critical [3]. A lack of process robustness and repeatability have been noted as two of the major barriers which prevents the full breakthrough of AM into risk-averse sectors [4, 5]. Thus, quality control in AM is an important issue which demands feasible solutions.

The current study focuses on laser powder bed fusion (L-PBF) processes (also known as Selective Laser Melting^{TM} and Direct Metal Laser Sintering^{TM}); AM technologies which produce complex metallic parts from powder materials. The L-PBF process is a cycle of three steps. First, a powder deposition system deposits a thin layer of metal powder ($20-60\mu$m thickness). A laser then melts the powder following a predefined scanning path [6]. The bed which holds the part is then lowered and the cycle is repeated.

Due to the layer-wise nature of the L-PBF process, defects are not always visible once the part has been completed. Consequently, expensive CT scans are often employed post-build to identify defects. By introducing an on-line process monitoring system, part quality could be monitored during the build. This would allow the operator to guarantee the quality of the resulting parts without using expensive CT measurements. At a later stage, such an on-line process monitoring system could, potentially, enable the implementation of automatic in-process corrective measures, thus facilitating process control for L-PBF. On-line process monitoring is also crucial for allowing the rapid qualification of parts in the R&D stage and to decrease machine downtime [7].

Several studies have already investigated the relationship between L-PBF process parameters, variations in photodiode signals and their affect on the final build quality. Bisht *et al.* [8] studied the correlation between sensor readings, taken from an off-axial photodiode, and tensile properties of L-PBF builds (ultimate tensile strength and plastic elongation). The work described in [9] explored the ability of two co-axial photodiode sensors to predict the ultimate tensile strength of L-PBF builds via a semi-supervised machine learning algorithm. The paper [10] analysed the ratio between two co-axial photodiode readings (ADC-1/ADC-2), that capture different near-infrared wavelengths, under different process conditions. According to their study both part density and photodiode signal ratio (ADC-1/ADC-2) gradually increase as the energy per unit volume (transferred to the material) increases up until 100% of part density. S. Coeck *et al.* [11] examined off-axial photodiode sensor readings, which measure the light emitted by the melt-pool, and identified porous structures within a L-PBF build by identifying abrupt fluctuations in the signal collected in adjacent scan vectors.

The aim of the current study is to investigate the feasibility of predicting L-PBF build quality, in terms of build density, using a combination of different co-axial photodiode sensor measurements collected during the build process. Build density (measured by OGP smartscope Zip Lite 300 at 75 magnification) is used to quantify the quality of the parts as it is a well-known indicator of global part quality [10]. It is noted that while many developmental on-line process monitoring systems employ images collected via cameras to detect defects in L-PBF builds [3, 12, 13, 14, 15, 16], using only photodiode measurements to monitor the build process is potentially beneficial as photodiode sensors are cost-efficient and typically have a higher sample rate compared to camera-based systems.

This study involves using a Singular Value Decomposition (SVD) to extract low-dimensional features from large datasets of photodiode measurements, so that the extracted features can then be fed into machine learning algorithms. The research exploits data collected during L-PBF builds fabricated in a Renishaw^{TM} AM 500M machine. Low density specimens are first identified via unsupervised clustering methods (K-means and a Gaussian mixture model (GMM)) before a supervised regression algorithm (Gaussian Process) is used to directly predict build density from the same extracted features.

This paper is organised as follows: Section 2 describes the motivation behind this research and discusses the state-of-the-art; Section 3 describes the feature extraction process and Section 4 introduces the machine learning methods used to cluster and predict the density of the L-PBF builds; Section 5 presents the results of the analysis. Finally, conclusions and suggestions for further extensions of the techniques are discussed in Section 6.

2. Literature Review

According to Mani *et al.* [17] and Yadroitsev *et al.* [18], there are over 50 process parameters which could affect the final quality of L-PBF builds. The laser serves as the energy source in the heat transfer process thus, parameters such as the peak power of the laser, pulse width, and pulse frequency impact the output of L-PBF builds. The focal point of the laser is moved across the build surface using a galvanometer scanner; the scan speed of the laser beam is also critical, as it impacts the energy applied to a particular spot of the build. Powder layer thickness, layer uniformity, powder temperature, and packing density can also significantly impact the heat transfer process [19].

There are several studies [10, 20] which demonstrate an association between the energy density transferred to the material and L-PBF build density. According to Gu *et al.* [20] the energy density (i.e. energy per unit volume) transferred to the material is given by

$$E = \frac{P}{vht} \tag{1}$$

where P is the laser power, v is the scan speed, t is the layer thickness and h is the hatch distance. Consequently, the studies [10, 20, 21, 22] focus on the influence of these parameters on build quality. Arisoy *et al.* [21] discusses the effect of scan strategy, laser power, scan speed and hatch distance on grain sizes and showed that increasing the energy density results in larger grain sizes. The work described in [22] has used scan speed and laser power to predict the porosity of metallic parts produced using L-PBF.

One common approach to melt-pool monitoring involves using camera-based sensing systems with CCD or CMOS detectors, which can achieve a relatively high spatial resolution. Such camera-sensing systems can allow evaluation of the temperature profile and shape of the melt-pool [23]. The optical set-up suggested by Kruth et al.[12] consisted of a high-speed NIR CMOS camera and a photodiode (sampling rate 10kHz) that was coaxial with the laser beam. Grasso *et al.* [3] utilised an off-axial camera sensing system with a CMOS detector which collected images at a rate of 300Hz. A pyrometer with an in-built CMOS detector (sampling rate 6.4Hz) was used by Khanzadeh *et al.* [13] to capture thermal images of the melt-pool.

Kruth *et al.* [12] suggested an approach for in-situ monitoring where the sensor measurements, taken from a high-speed NIR CMOS camera and a photodiode, were mapped into interpretable process-quality images with a relatively high response rate (10kHz). Mapped sensor data, with the intensity and the area of each melt-pool, were examined for anomalies using pre-defined expected values. This system requires a position-dependent reference database unique to each part, generated by traditional validation techniques in order to generate those expected values for different scanning patterns (i.e. fill and contour). While the study stated that there is an excellent compatibility between the detected errors and actual defects, the statistical significance of this study has not been reported.

A recent study carried out by Grasso *et al.* [3] used principal component analysis to compress image data of the melt-pool (collected via an off-axial camera sensing system) and output a statistical descriptor that can be used to identify defect areas. The proposed method was able to automatically detect and localise a defect during the layer-by-layer L-PBF process. However, the statistical significance of this study has not been reported.

A real-time porosity prediction method was developed by Khanzadeh *et al.* [13], using morphological characteristics of the melt-pool boundary. The suggested method used a polar transformation to convert Cartesian co-ordinates of the melt-pool boundaries into polar co-ordinates (ρ and θ). Once the polar transformed melt-pool contour were represented using a function ($\rho = g(\theta)$, where $\theta \in (-\pi, \pi)$), functional principal component analysis (FPCA) was used to fit a smooth functional curve and extract critical features to classify defective and non-defective melt-pools. An accuracy level of

98.44% was realised in classifying melt-pools obtained during fabrication of a thin wall structure. However, this approach had a relatively slow response rate due to the use of a camera-based monitoring system.

The studies [14, 15, 16] utilised off-axial high resolution imaging, obtained through visual cameras, to detect anomalies in L-PBF build layers. Aminzadeh *et al.* [14], captured build images using a 8.8 megapixel USB digital camera with high focus lenses and Gobert *et al.* [15] used a 36.3-megapixel DSLR camera (Nikon D800E) to take multiple images of the build layers.

The method suggested by Aminzadeh *et al.* [14], used a database of camera images with pre-identified zones (Zone I being the range where parts with no noticeable pores are created, Zone II being the 'high-energy zone' where small spherical, gas pores are created, and Zone III being 'low-energy zone' where large irregular pores and lack of fusion occur) in layers of AM parts made with varying part quality, to train a Bayesian classifier. Appropriate features were selected by taking texture characteristics into consideration and by converting the images into the frequency domain. The developed Bayesian classifier was able to achieve a 89.5% true positive rate and 82% true negative rate. However, as the high resolution images being used captured the entire build layer, significant image post-processing was required to correct for image contrast between the part and powder.

Gobert *et al.* [15] proposed a method to identify discontinuities (e.g. porosity, cracks), in which the co-ordinates of anomalies and nominal voxels in the CT scan domain were matched with layer-wise images. Features extracted from this matching layer-wise image stack were employed to train a binary classifier. Discontinuities were detected with an 80% success rate, however the approach heavily relied on embedded reference points for the calibration of coordinate transformations.

In the study conducted by Guo *et al.* [24] predictions of the melt-pool shape and dimensions were made using a 3D finite element model. However, the study suggests a rather complex model which makes the analysis time consuming and difficult to apply.

Table 1 summarises some of the state-of-the-art in-situ monitoring systems designed for the L-PBF build process. Table 1 also reports the data processing and analysis techniques utilised in those systems.

doi:10.20944/preprints202004.0055.v1

Table 1: Selected literature on in situ monitoring for automated defect detection in L-PBF

Reference	Process signature	Data processing technique	Analysing technique
Kruth *et al.* [12]	Melt-pool geometry and plume characteristics	Sensor data processed by a FPGA chip is mapped into a 2D regular grid, according to their logged positions, to assign the melt-pool data to a particular pixel	Statistical Process Control is carried out with reference data, generated by previous built parts using traditional validation techniques (CMM, CT, Archimedes, microscope)
Grasso *et al.* [3]	Melt-pool geometry and plume characteristics	A statistical descriptor based on principal component analysis (PCA) is applied to image data, which is suitable for identifying defective areas within a layer	K-means Clustering for Automated Defect Detection
Fu *et al.* [24]	Temperature profile	A 3D finite element thermal model was developed to investigate the thermal process of L-PBF using commercial software ABAQUS	Melt-pool shape and dimensions was predicted using process parameters and then verified with previously collected experimental data
Khanzadeh *et al.* [13]	Melt-pool geometry and temperature profile	Polar transformation was applied to position co-ordinates of the melt-pool boundaries and then functional principal component analysis (FPCA) was performed to extract key characteristics of those boundaries	Four different methods were used for melt-pool classification: K-nearest neighbour, support vector machine, decision tree, discriminant analysis

Continued on next page

Table 1 – *Continued from previous page*

Reference	**Process signature**	**Data processing technique**	**Analysing technique**
Foster *et al.* [25]	Plume characteristics	Images of layers were taken both immediately after re-coating and after laser exposure	Post-processed and analyzed images were stacked to create 3D models to find anomalies
Craeghs *et al.* [16]	Plume characteristics	Melt-pool length and width of the captured melt-pool images were determined using image processing algorithms with the help of a FPGA chip	Change in length to width ratio is used detect process abnormalities
Aminzadeh *et al.* [14]	Plume characteristics	Features, carefully selected based on physical intuition into the process, were extracted from the images of L-PBF builds	Extracted features were classified using a Bayesian classifier
Gobert *et al.* [15]	Plume characteristics	Multi-dimensional visual features were extracted from layer-wise image stacks	Extracted features were evaluated using binary classification techniques, i.e. a linear support vector machine (SVM)
Coeck *et al.* [11]	Plume characteristics	Identifying position co-ordinates of melt-pools where the signal is fluctuating within a scan vector	Identified defective melt-pools within close proximity were utilsed to detect defective

Of the aforementioned work, [8, 9, 10, 11] utilised photodiode sensors. Photodiodes are spatially integrated single-channel detectors that provide a voltage corresponding to the amount of light collected by the detector at each focal point. Cost effectiveness, high sensitivity, robustness, and fast data collection rates (typically $\sim$ 50kHz) make these devices attractive for L-PBF in-process monitoring. These sensors are, however, typically sensitive only over a limited range of wavelengths. Thermal radiation from the melt-pool is generally in the visible to IR range (900 to 2300 nm) while plasma emission is near UV or visible wavelengths (400 to 650 nm) [26]. Photodiodes simplify the data processing, relative to a camera-sensing system. On the other hand, camera-sensing systems provide a more detailed overview of the melt-pool characteristics. Consequently, choosing a sensor system for melt-pool monitoring is a trade-off between the response rate, cost and usefulness of the data that can be collected. Thus, many studies ([12, 23, 27], for example) exploit both photodiodes and CCD or CMOS cameras to capture the process dynamics of the melt-pool. However, the response rate of the monitoring system decreases as the response rate of a camera system is quite low compared to that of photodiodes [1].

The current study explores the feasibility of using a set of measurements collected through different co-axial photodiode sensors to predict the density of L-PBF builds. The overall aim of this paper, then, is to develop a model that can predict L-PBF build quality via build-data acquired through photodiode sensors.

3. Feature Extraction

A Renishaw^{TM} AM 500M machine was utilised to build the test samples used in this study. The machine sensor system, shown in Figure 1, consists of two high precision co-axial single-channel detectors that are designed to capture melt-pool plume characteristics.

Photodiode-1 (PD1 - no. 4 in Figure 1, wavelength - 700 to 1050 nm) is sensitive to plasma emissions whereas photodiode-2 (PD2 - no. 5 in Figure 1, wavelength - 1080 to 1700 nm) is sensitive to thermal radiation. A third photodiode, photodiode-3 (PD3 - no. 10 in Figure 1) measures the intensity of the laser beam. The optical window (no.16 in Figure 1), which helps focus the laser beam, exhibits $>$ 95% spectral transmission across the wavelength of interest. The machine has a Galvo-scanner system (no. 19 in

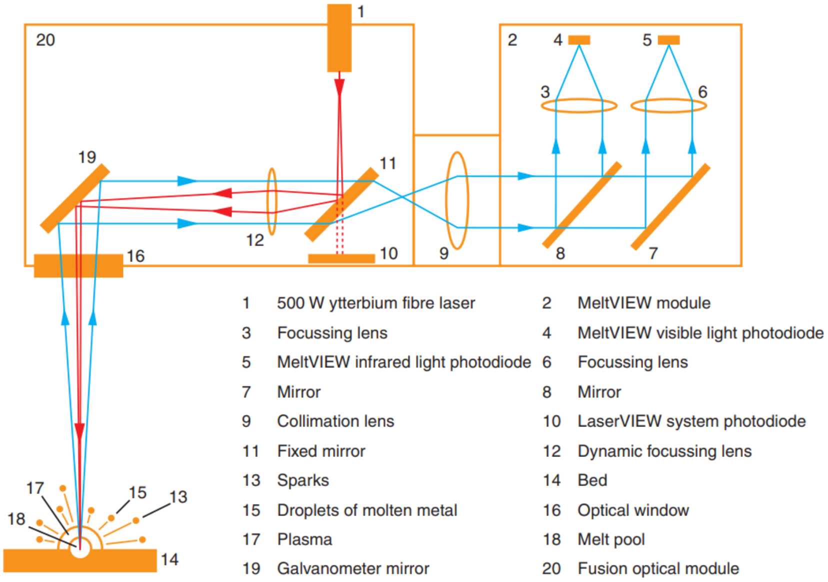

1	500 W ytterbium fibre laser	2	MeltVIEW module
3	Focussing lens	4	MeltVIEW visible light photodiode
5	MeltVIEW infrared light photodiode	6	Focussing lens
7	Mirror	8	Mirror
9	Collimation lens	10	LaserVIEW system photodiode
11	Fixed mirror	12	Dynamic focussing lens
13	Sparks	14	Bed
15	Droplets of molten metal	16	Optical window
17	Plasma	18	Melt pool
19	Galvanometer mirror	20	Fusion optical module

Figure 1: Renishaw^{TM} AM 500M machine schematic assembly of the optical sensing system (image reproduced with permission from the Renishaw Brochure ‘InfiniAM Spectral’, available at http://www.renishaw.com/en/infiniam-spectral–42310).

Figure 1) which controls the movement of the laser focal point, such that it follows pre-defined (x, y) coordinates. In the following experiments, the (x, y) coordinates of the laser focal point were collected at 100 kHz alongside the photodiode measurements.

Sixty-two cubes (Figure 2(a)) were built using different combinations of process parameters (i.e. laser power, scan speed and hatch distance) according to a Design of Experiments (DoE) procedure. This DoE procedure was carried out following standard practice implemented by Renishaw. Figure 2(b) shows the (x, y) coordinates of the laser point over a single layer (the first layer created after the initial support layers) of the build. To filter the sensor measurements, data points recorded when the laser was off (when the laser was moving in between specimens and in between hatches) and when the laser was used on contours (edge of each specimen) were removed from the analysis. The data was further filtered by extracting only the maximum intensity of the laser beam per each exposure. The sensor data was separated into 62 data sections, each corresponding to a single

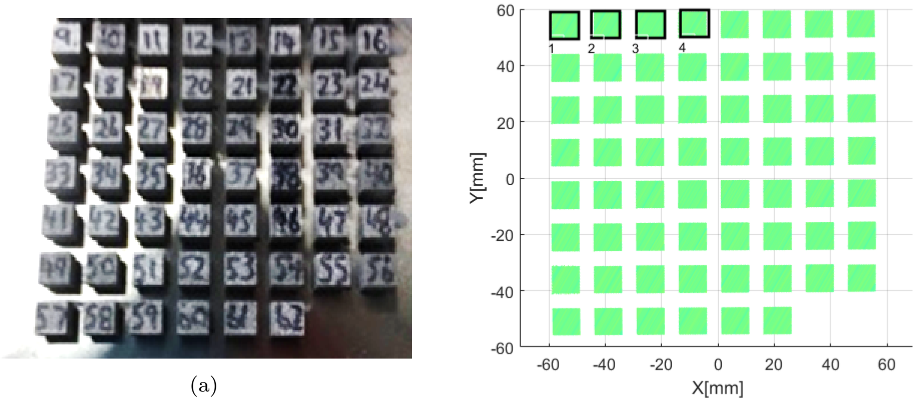

(a)

(b)

Figure 2: (a) 62 cubes built with different combinations of process parameters (laser power, scan speed and hatch distance) (b) (x, y) coordinates of the laser point representing a single layer of the build shown in (a).

cube. The data separation was carried out by creating polygons marking the boundaries of each cube (see black outlines in Figure 2(b)) and then indexing all the data points within each area as a single section. Examples of the resulting data segments are shown in Figure 3(a). Even though some data was removed when a single reading per exposure were extracted, the number of data points corresponding to each cube was recorded separately, as this value is proportional to the time spent by the laser on each bounded area; the number of data points collected per cube is shown in Figure 3(b). Subsequently, for each photodiode, the sensor data recorded for each cube was arranged into separate columns, creating three separate data matrices (one per photodiode). To ensure that these matrices had the same number of elements in each column, the minimum column length across each specimen was determined and then the data was truncated accordingly. Each of the resulting data matrices were of dimension 1216×62. A Singular Value Decomposition (SVD) was then performed on each data matrix to extract the features that, later in this study, are used as inputs to various machine learning approaches.

In the following, to illustrate the feature extraction procedure, we use $\boldsymbol{A}$ to denote a data matrix obtained from one of the 3 photodiode sensors. An SVD takes a data matrix, $\boldsymbol{A}$, and factorises it into a product of three

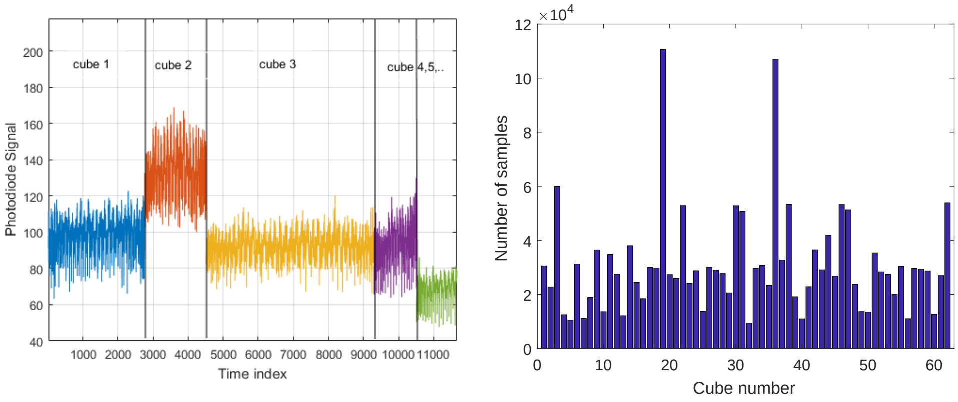

(a)

(b)

Figure 3: (a) The separation of the data was carried out by indexing all the data points with respect to their location on the layer. (b) The number of samples collected while building each cube.

separate matrices:

$$\boldsymbol{A} = \boldsymbol{U}\boldsymbol{S}\boldsymbol{V}^T \tag{2}$$

If the original data matrix $\boldsymbol{A}$ is $(m \times n)$, then $\boldsymbol{U}$ will be an $(m \times m)$ orthonormal matrix and $\boldsymbol{V}$ will be a $(n \times n)$ orthonormal matrix. $\boldsymbol{S}$, an $(m \times n)$ matrix, has the form

$$\boldsymbol{S} = \begin{bmatrix} \boldsymbol{\Sigma} \\ \boldsymbol{0} \end{bmatrix}, \qquad \boldsymbol{\Sigma} = \mathrm{diag}(S_1, S_2, ..., S_n) \tag{3}$$

where the diagonal elements of $\boldsymbol{\Sigma}$ are sorted from largest to smallest. These diagonal elements are the square root of the eigenvalues of $\boldsymbol{A}\,\boldsymbol{A}^T$ and are commonly referred to as ‘singular values’.

As a result of the SVD, each column of $\boldsymbol{A}$ can be expressed as a linear combination of basis vectors $(\boldsymbol{u}_1, \boldsymbol{u}_2, ..., \boldsymbol{u}_m)$. Specifically, by defining $\boldsymbol{C} = \boldsymbol{S}\,\boldsymbol{V}^T$, one can write

$$\boldsymbol{A} = \boldsymbol{U}\,\boldsymbol{C} \Rightarrow \boldsymbol{a}_i = \sum_{j=1}^{m} \boldsymbol{u}_j\, C_{j,i} \tag{4}$$

where $\boldsymbol{a}_i$ is the i^{th} column of $\boldsymbol{A}$ and $\boldsymbol{u}_j$ is the j^{th} column of $\boldsymbol{U}$. Thus, each vector $\boldsymbol{a}_i$ is now associated with a constant $C_{j,i}$ for every basis vector

$\boldsymbol{u}_j$. Often, only a small subset of singular values are significantly different from zero. In such cases, the sum in equation (4) can be truncated and each column of $\boldsymbol{A}$ can be well approximated using only a limited number of $k < m$ basis vectors, $\boldsymbol{u}_1, \boldsymbol{u}_2, ..., \boldsymbol{u}_k$. Specifically, by writing $\bar{\boldsymbol{C}} = \boldsymbol{S}_k \boldsymbol{V}_k^T$ where $\boldsymbol{V}_k$ is a $(n \times k)$ matrix, composed of the first k columns of $\boldsymbol{V}$, and $\boldsymbol{S}_k$ represents a $(k \times k)$ matrix which includes the first k singular values $(S_1, S_2 .... S_k)$:

$$\boldsymbol{A} \approx \bar{\boldsymbol{A}} = \boldsymbol{U}_k \bar{\boldsymbol{C}} \Rightarrow \bar{\boldsymbol{a}}_i = \sum_{j=1}^{k} \boldsymbol{u}_j \bar{C}_{j,i} \tag{5}$$

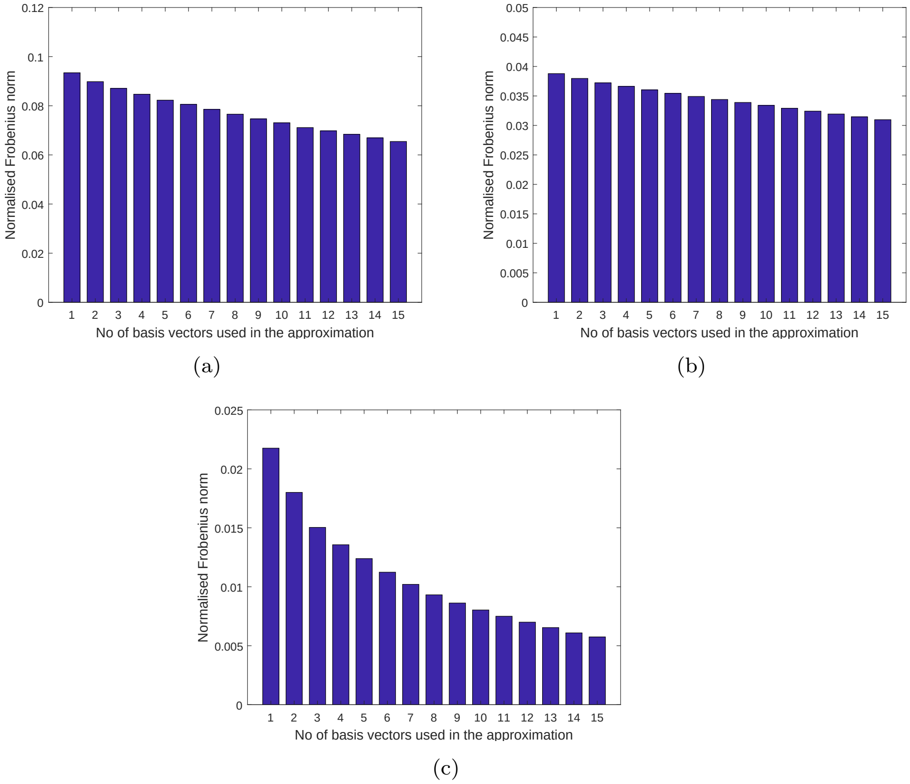

(a)

(b)

(c)

Figure 4: Normalised Frobenius norm for the Photodiode-1 (a), Photodiode-2 (b) and Photodiode-3 (c) data matrices. The first 15 basis vectors are shown (out of a total of 1216 basis vectors).

The difference between $\boldsymbol{A}$ and $\bar{\boldsymbol{A}}$ can be quantified using the normalised

Frobenius norm [28]:

$$\|\boldsymbol{A} - \bar{\boldsymbol{A}}\|_{\text{Fro}} = \sqrt{\frac{\Sigma_{i=1}^{n}\Sigma_{j=1}^{m}(\mid a_{j,i} - \bar{a}_{j,i} \mid / \mid a_{j,i} \mid)^2}{mn}} \tag{6}$$

For each of the three data matrices, the number of basis vectors (k) employed for generating the approximated matrix $\bar{\boldsymbol{A}}$ was increased up until k=15 and the Frobenius norm was used to quantify the contribution of each basis vector to the information contained in the original matrix $\boldsymbol{A}$. Figure 4 shows how the Frobenius norm decreases as the number of basis vectors increases for all three data matrices. It can be seen that the approximation realised using only the first basis vector captures most of the data - in fact, the Frobenius norm for photodiode-1 is only 0.0934 (for context the Frobenius norm when $\bar{\boldsymbol{A}} = \boldsymbol{0}$ is 1). Similarly, the Frobenius norm for photodiode-2 and photodiode-3, using 1 basis vector only, is 0.0388 and 0.0218 respectively. In the following, the constants relating to the first basis vectors of the three matrices are therefore used as the extracted features to be inputted into the machine learning algorithms.

4. Algorithm Descriptions

This section describes the supervised and unsupervised machine learning approaches that were used in the current study. The features considered here are the constants $C_{j,i}$ (defined in equation (5)) that are related to the first basis vectors of photodiode-1, photodiode-2 and photodiode-3, as well as the total number of scan samples used within each bounded area (as it is proportional to the time spent by the laser on each specimen). Herein, all the components of the feature space are represented by the vector $\boldsymbol{x}_i = \left[x_i^{(1)} . \ . \ x_i^{(D)}\right]^T$, where D is the dimension of the feature space and i is used to index each specimen. As an example, $\boldsymbol{x}_i$ can be a combination of $C_{1,i}^{PD1}$, the constants that are related to the first basis vectors of photodiode-1 and $C_{1,i}^{PD2}$, the constants that are related to the first basis vectors of photodiode-2, which provides a 2D feature space (such that $D = 2$). All the feature vectors were normalised by subtracting the mean value and dividing by the standard deviation.

In the current work, the ability of two different unsupervised learning approaches (K-means clustering and a Gaussian Mixture Model (GMM), described in Section 4.1) to cluster the feature space was assessed. Subsequently, it was investigated whether supervised regression could be used to

doi:10.20944/preprints202004.0055.v1

directly predict sample density using the same feature vectors. This was investigated using a Gaussian Process (GP) regression algorithm with Automatic Relevance Determination, which is described in Section 4.2.

4.1. Unsupervised learning

The two unsupervised approaches used in this study are briefly explained below.

4.1.1. K-means algorithm

Given a set of n observations $\{\boldsymbol{x}_1, \boldsymbol{x}_2, \ldots, \boldsymbol{x}_n\}$ (in this case representing n points in the feature space, $n = 62$), K-means clustering aims to partition the observations into sets $\boldsymbol{h}_r = \boldsymbol{h}_1, \boldsymbol{h}_2, \ldots, \boldsymbol{h}_q$ $(q \leq n)$. The K-means algorithm begins with an initial estimate of cluster centres ($\boldsymbol{o}_r$ where $r = 1, 2..., q$) before calculating the distance between each point and each centre. Each observation is then assigned to the cluster whose centre is closest. In the next iteration of the algorithm, the centres are recomputed by setting them equal to the mean of the newly classified points. The process of estimating cluster centres and assigning observations to clusters is then repeated until the cluster centers are judged to have converged. The interested reader can can refer to [29] for further details.

4.1.2. Gaussian Mixture Model

K-means is a deterministic approach, based on the assumption of spherical clusters. Gaussian Mixture Models (GMMs) are probabilistic and can be used to identify non-spherical clusters. GMMs therefore provide more flexibility compared to the K-means algorithm. With a GMM it is assumed that each feature vector has been generated from one of H Gaussian distributions, such that

$$p(\boldsymbol{x}_i) = \sum_{c=1}^{H} \pi_c \mathcal{N}(\boldsymbol{x}_i \mid \boldsymbol{\mu}_c, \boldsymbol{\Sigma}_c) \tag{7}$$

where the π_c's are called *mixture proportions* and c indexes each cluster. The parameters $\boldsymbol{\mu}_c$ and $\boldsymbol{\Sigma}_c$ represent the mean and the covariance matrix of the c^{th} cluster respectively.

Training a GMM involves inferring estimating the parameters, $\boldsymbol{\theta}_{GMM} = \{\pi_c, \boldsymbol{\mu}_c, \boldsymbol{\Sigma}_c\}$, where $c = 1, 2, ..., H$, which maximises the likelihood of witnessing the data $\boldsymbol{x}_1, .., \boldsymbol{x}_n$. This estimation procedure is typically undertaken using the Expectation Maximisation (EM) algorithm, which consists

doi:10.20944/preprints202004.0055.v1

of two main steps: the expectation step (E-step) and the maximization step (M-step). The EM algorithm begins by randomly initialising the GMM parameters for each cluster. Given these parameters, the posterior probability that cluster c is responsible for generating $\boldsymbol{x}_i$ is calculated as part of the E-step. To do so, let us assume that each data point $\boldsymbol{x}_i$ is given a 'label' $\boldsymbol{z}_i \in \mathbb{R}^H$ describing which Gaussian was used to generate it, where the labels are such that $z_{c,i} \in \{0, 1\}$ subject to $\sum_{c=1}^{H} z_{c,i} = 1, \quad \forall i$. These labels are hidden to the user (and are therefore named 'latent variables') and determine the cluster from which each observation originates ($z_{c,i} = 1$ means that the point x_i came from the $c^{\text{ th}}$ Gaussian with probability 1). The expected value of $z_{c,i}$, at the $t^{\text{ th}}$ iteration of the algorithm, is

$$\gamma(z_{c,i})^{(t)} = \frac{\pi_c \mathcal{N}(\boldsymbol{x}_i \mid \boldsymbol{\mu}_c, \boldsymbol{\Sigma}_c)}{\sum_{c'=1}^{H} \pi_{c'} \mathcal{N}(\boldsymbol{x}_{\boldsymbol{i}} \mid \boldsymbol{\mu}_{c'}, \boldsymbol{\Sigma}_{c'})} \tag{8}$$

Fixing each $z_{c,i}$ equal to its expected value, in the M-step, a new set of parameters for the Gaussian distributions are computed such that they maximise the lower bound of the log likelihood of all the observations in each cluster. This is called the M-step. It can be shown that the maximum likelihood parameters are

$$\boldsymbol{\mu}_c^{(t+1)} = \frac{1}{n_c} \sum_{i=1}^{n} \gamma(z_{c,i})^{(t)} \, \boldsymbol{x}_i \tag{9}$$

$$\boldsymbol{\Sigma}_c^{(t+1)} = \frac{1}{n_c} \sum_{i=1}^{n} \gamma(z_{c,i})^{(t)} (\boldsymbol{x}_i - \boldsymbol{\mu}_c^{(t+1)})(\boldsymbol{x}_i - \boldsymbol{\mu}_c^{(t+1)})^T \tag{10}$$

$$\pi_c^{(t+1)} = \frac{n_c}{n} \tag{11}$$

where

$$n_c = \sum_{i=1}^{n} \gamma(z_{c,i})^{(t)} \tag{12}$$

Once these parameters are calculated, the log likelihood is evaluated as follows

$$\ln p(\boldsymbol{x}_1, ..., \boldsymbol{x}_n \mid \boldsymbol{\mu}, \boldsymbol{\Sigma}, \boldsymbol{\pi}) = \sum_{i=1}^{n} \ln \left\{ \sum_{c=1}^{H} \pi_c \mathcal{N}(\boldsymbol{x}_i \mid \boldsymbol{\mu}_c, \boldsymbol{\Sigma}_c) \right\} \tag{13}$$

Equation (13) can be used to analyse convergence of the EM algorithm as it runs over a number of iterations.

doi:10.20944/preprints202004.0055.v1

4.2. Supervised learning

In Supervised Learning, algorithms learn from labeled data. The approach used in this study, namely Gaussian Process regression, is briefly explained below.

4.2.1. Gaussian Process Regression

Let us assume there exists a function that can predict the density, d, of each specimen from the extracted features $\boldsymbol{x}$. However, that function is unknown and regression is used to estimate it from the data. Here, it is assumed that

$$d_i = f(\boldsymbol{x}_i) + \epsilon, \qquad \epsilon \sim \mathcal{N}(\epsilon; 0, \sigma^2) \tag{14}$$

such that each observation, d_i, is equal to the function f evaluated at input $\boldsymbol{x}_i$ but corrupted with zero mean Gaussian noise of variance σ^2. By defining

$$\boldsymbol{f} = (f_1, f_2 ......, f_n)^T, \qquad f_i \equiv f(\boldsymbol{x}_i) \tag{15}$$

then, from the definition of a Gaussian process, $p(\boldsymbol{f})$ is a Gaussian whose mean is zero and whose co-variance is defined by a Gram matrix, $\boldsymbol{K}$, so that

$$p(\boldsymbol{f}) = \mathcal{N}(\boldsymbol{f}; \boldsymbol{0}, \boldsymbol{K}) \tag{16}$$

The matrix $\boldsymbol{K}$ is defined using a kernel function, k, chosen to ensure that $\boldsymbol{K}$ is a valid covariance matrix. In this study, the considered kernel [29] is

$$k(\boldsymbol{x}, \boldsymbol{x}') = \exp\left(-\frac{1}{2} \sum_{j=1}^{D} \frac{1}{L_j^2} (x_j - x_j')^2 \right) \tag{17}$$

where x_j represents the j^{th} component of $\boldsymbol{x}$.

The 'hyperparameters', L_j $(j = 1, ..., D)$ and σ are collected together into the vector $\boldsymbol{\theta}_{GP}$=$\{ L_1, L_2, ..., L_D, \sigma\}$. The hyperparameter L_j controls the lengthscale of the kernel function for the j^{th} input dimension. By allowing different lengthscales for each dimension of the input space, it is possible to control the sensitivity of the regression to each model input. The identification of the hyperparameteres $L_1, ..., L_d$ is referred to as Automatic Relevance Determination (ARD), as it helps one to establish the relevance of different inputs to the model predictions. If, for example, the j^{th} feature has no relevance for the regression problem, the optimum lengthscale, L_j, will be relatively large (thus reducing the sensitivity of the regression model to that feature). ARD can therefore be used to discard features that are less relevant.

From the noise model (equation (14)), the likelihood of observing $\boldsymbol{d} = (d_1, ..., d_n)^T$, conditional on $\boldsymbol{f}$, is

$$p(\boldsymbol{d}\,|\boldsymbol{f}) = \mathcal{N}(\boldsymbol{d}; \boldsymbol{f}, \boldsymbol{I}\sigma^2) \tag{18}$$

where $\boldsymbol{I}$ is the identity matrix. By marginalising over $\boldsymbol{f}$, the marginal likelihood is

$$p(\boldsymbol{d}) = \int p(\boldsymbol{d}\,|\boldsymbol{f})p(\boldsymbol{f})d\boldsymbol{f} = \mathcal{N}(\boldsymbol{d}; \boldsymbol{0}, \boldsymbol{K} + \sigma^2\boldsymbol{I}) \tag{19}$$

Given the training dataset, the optimum parameters $\boldsymbol{\theta}_{GP}$ which maximise the marginal log likelihood can be estimated using gradient-based optimisation algorithms (e.g. conjugate gradients [30]). Once the optimum parameters are identified, in response to a new input $\boldsymbol{x}_*$ (generated using a build that was not included in the training data, for example), the probability that this sample has measured density d_* is given by

$$p(d_*|\,\boldsymbol{d}) = \mathcal{N}(d_*|m_*, \sigma_*^2) \tag{20}$$

where

$$m_* = \boldsymbol{k}^T\,\boldsymbol{C}^{-1}\,\boldsymbol{d}, \qquad \sigma_*^2 = \sigma^2 + k(\boldsymbol{x}_*, \boldsymbol{x}_*) - \boldsymbol{k}^T\,\boldsymbol{C}^{-1}\,\boldsymbol{k}\,. \tag{21}$$

and

$$\boldsymbol{C} = \boldsymbol{K} + \sigma^2\boldsymbol{I}, \qquad \boldsymbol{k} = k(\boldsymbol{x}_i, \boldsymbol{x}_*) \quad i = 1, 2, ...n \tag{22}$$

5. Results and Discussion

As mentioned in Section 4, the constants relating to the first basis vectors of the data matrices of Photodiode-1 ($C_{1,i}^{PD1}$), Photodiode-2 ($C_{1,i}^{PD2}$), Photodiode-3 ($C_{1,i}^{PD3}$) and the total number of scan samples (T_i) of each specimen were used to create the feature space.

Table 2: Recognising clusters in the 2D feature space

Extracted features				Evident clusters
$C_{1,i}^{PD1}$	$C_{1,i}^{PD2}$	$C_{1,i}^{PD3}$	T_i	
●	●			X
●		●		X
	●	●		X
●			●	✓
	●		●	X
		●	●	✓

Initially, all the combinations of feature pairs were taken into consideration. Figure 5 shows several combinations of pairs of feature vectors, plotted on a 2-dimensional space, where the data points have been coloured depending on the density of each specimen. The specimens with a density higher than or equal to 99% were categorised as high density parts (green triangles) and the specimens with a density less than 99% were categorised as low density parts (red circles).

When observing the distribution of data points in Figure 5, it was evident that when the coefficients relating to the first basis vector of photodiode-2 ($C_{1,i}^{PD2}$) and photodiode-3 ($C_{1,i}^{PD3}$) were plotted with the coefficients relating to the first basis vector of photodiode-1 ($C_{1,i}^{PD1}$) (Figure 5(a) and Figure 5(b)) or when $C_{1,i}^{PD2}$ and $C_{1,i}^{PD3}$ were plotted against each other (Figure 5(c)), the categories of density did not appear in separate clusters. Again, when $C_{1,i}^{PD2}$ were plotted against the total number of scan samples (T_i), there were no evident clusters (Figure 5(e)). However, when $C_{1,i}^{PD1}$ were plotted against T_i (Figure 5(d)), the categories of density appeared to be better separated. Furthermore, when $C_{1,i}^{PD3}$ were plotted against T_i, there were also roughly recognisable clusters (Figure 5(f)). The capability of these feature combinations to separate the data points into clusters is summarised in Table 2.

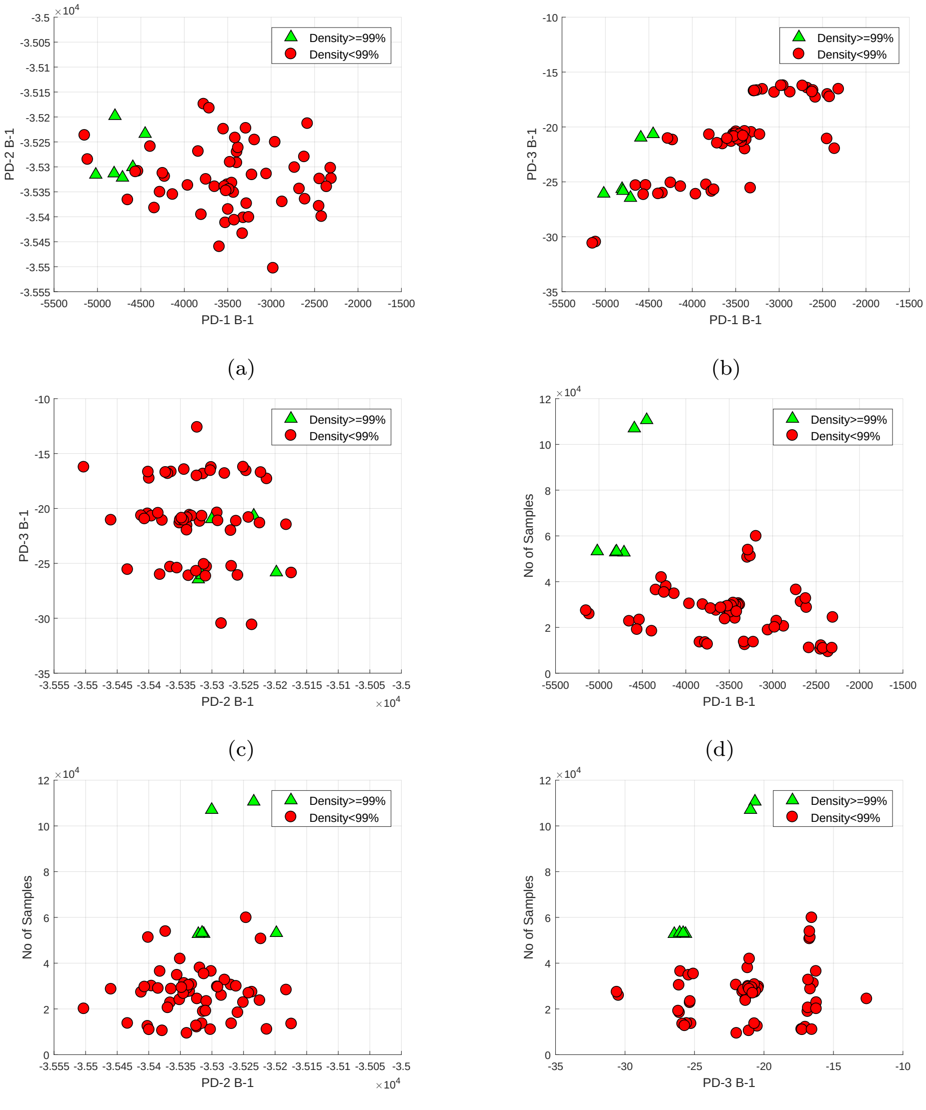

(a) (b) (c) (d) (e) (f)

Figure 5: (a) $C_{1,i}^{PD1}$ plotted against $C_{1,i}^{PD2}$ (b) $C_{1,i}^{PD1}$ plotted against $C_{1,i}^{PD3}$ (c) $C_{1,i}^{PD2}$ plotted against $C_{1,i}^{PD3}$ (d) $C_{1,i}^{PD1}$ plotted against T_i (e) $C_{1,i}^{PD2}$ plotted against T_i (f) $C_{1,i}^{PD3}$ plotted against T_i

doi:10.20944/preprints202004.0055.v1

5.1. Unsupervised learning

The feature combinations with recognisable clusters ($C_{1,i}^{PD1}$ plotted against T_i and $C_{1,i}^{PD3}$ plotted against T_i) were used as input features for the unsupervised machine learning algorithms. It is noted that the number of samples was always included in the feature space. For the sake of completeness, several features were added to the feature pairs recognised in the previous stage to be successful in separating categories of densities, creating both 3D and 4D feature spaces.

In the following, 50% of the available data was used for algorithm training such that the remaining 50% was used to test each algorithm's predictive capabilities. The training and testing data consisted of 31 data points each. 2-fold cross validation was performed whereby the role of the two datasets was reversed (such that the training data became the testing data and *vice-versa*) before the predictive ability for each fold was averaged to estimate the final accuracy level. Specifically, the average accuracy level was calculated as

$$\text{Avg. success rate\%} = \frac{\sum_{i=1}^{2}\left(\frac{N_{\text{correct},i}}{N_{\text{total},i}}\right)\times 100}{2} \tag{23}$$

where $N_{\text{correct},i}$ is the number of correctly predicted specimens and $N_{\text{total},i}$ is the total number of specimens in the i^{th} fold.

We note that, with the GMM, the 'threshold probability' was set equal to 0.5 such that, if the probability of a particular data point being in one particular cluster is more than 0.5, the point is considered part of that cluster.

All the combinations used to create the feature space and the obtained accuracy levels are provided in Table 3. We used K-means first to cluster the feature space as it is a relatively simple approach and because the produced results provide a good reference to validate the subsequent GMM results. Referring to Table 3, it can be observed that, in the case of the GMM, the highest success rate (93.54%) was achieved when $C_{1,i}^{PD1}$ and T_i were used as input features. The same success rate was obtained when $C_{1,i}^{PD3}$ and T_i were used as input features. Comparing the results obtained with K-means clustering for those feature pairs, the highest accuracy were given when $C_{1,i}^{PD1}$ and T_i were used as input features. However, adding $C_{1,i}^{PD2}$ to that feature pair ($C_{1,i}^{PD1}$ and T_i) was detrimental as the success rate of both

Table 3: Accuracy in classification calculated using (23)

Extracted features				K-means	GMM
$C_{1,i}^{PD1}$	$C_{1,i}^{PD2}$	$C_{1,i}^{PD3}$	T_i		
✓			✓	80.65%	93.54%
		✓	✓	77.42%	93.54%
✓	✓		✓	74.19%	79.03%
	✓	✓	✓	83.87%	83.87%
✓		✓	✓	75.81%	90.03%
✓	✓	✓	✓	66.13%	79.03%

clustering techniques was reduced with the introduction of the new feature. Adding coefficients relating to $C_{1,i}^{PD3}$ to the same feature pair ($C_{1,i}^{PD1}$ and T_i) also slightly reduced the success rate of both clustering techniques. Therefore, in the following, we use the features relating to PD-1 and number of samples ($C_{1,i}^{PD1}$ plotted against T_i) to quantify the performance of the GMM.

For illustrative purposes, Figure 6 and Figure 7 show the results obtained for validation data in the first and second fold, respectively, when T_i and $C_{1,i}^{PD1}$ were clustered using the GMM. Figures 6(a) and 7(a) illustrate the measured part density (parts with high density in green and low density in red) while Figures 6(b) and 7(b) illustrate the GMM results.

To further quantify the performance of the GMM, a Receiver Operating Characteristic (ROC) curve was created. A Receiver Operating Characteristic curve is a graphical plot that illustrates the diagnostic ability of a probabilistic classification algorithm as the algorithm's threshold probability is varied from 0 to 1. To create a ROC curve, a classifier's False Positive Rate (FPR) and True Positive Rate (TPR) are recorded for a range of different threshold probabilities before being plotted against each another. For the current example, the TPR is defined as the ratio of correctly identified low density parts, relative to the total number of low density parts. Likewise, the FPR is defined as the ratio of falsely identified low density parts, relative to the total number of high density parts. The Area Under the Curve (AUC) represents a measure of separability. The higher the AUC is or the closer the curve is to the top-left of the plot, the better the model is at distinguishing between parts with high density and low density. AUC=0.5

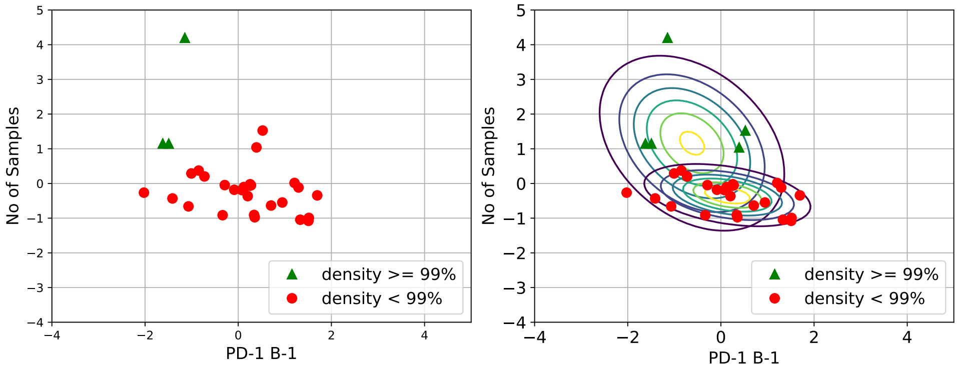

(a) (b)

Figure 6: Combinations of feature vectors, plotted in a 2-dimensional space, where the data points have been coloured depending on the density of the each specimen. $C_{1,i}^{PD1}$ vs. T_i plotted for the validation data in the first fold of the cross-validation. (a) The colour green represents samples with measured density $\geq 99\%$ and red represents samples with measured density $< 99\%$. (b) The colour green represents cluster-1 (predicted density $\geq 99\%$) and red represents cluster-2 (predicted density $< 99\%$).

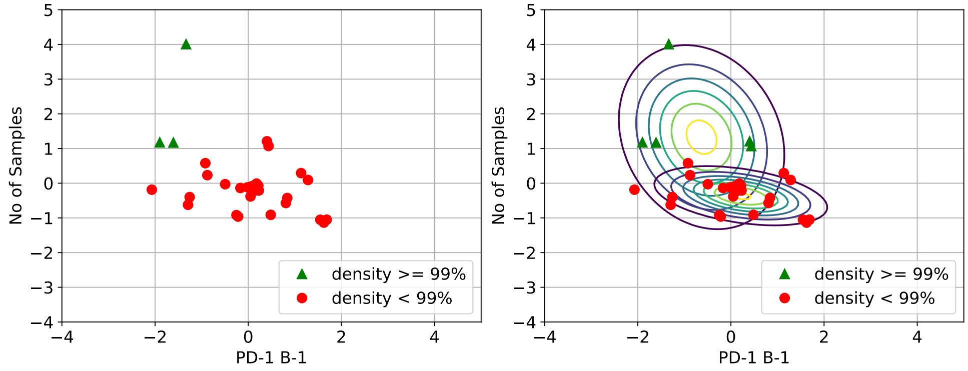

(a) (b)

Figure 7: $C_{1,i}^{PD1}$ vs. T_i plotted for the validation data in the second fold of the cross-validation. (a) The colour green represents samples with measured density $\geq 99\%$ and red represents samples with measured density $< 99\%$. (b) The colour green represents cluster-1 (predicted density $\geq 99\%$) and red represents cluster-2 (predicted density $< 99\%$).

indicates that the model has no class separation capacity, while AUC=1.0 indicates that the model can separate the classes with 100% accuracy.

In order to analyse the performance of the GMM for a variety of threshold probabilities, an ROC curve was plotted for the case where the feature space consisted of $C_{1,i}^{PD1}$ and T_i. The results obtained in both folds of the validation data were used to plot the ROC curve shown in Figure 8. The AUC value for both first fold and second fold is 0.946, which indicates that GMM is capable of accurately classifying parts according to their densities for a range of threshold probabilities.

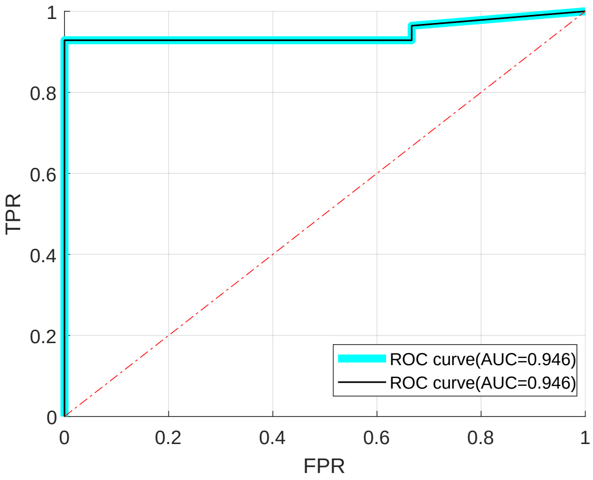

Figure 8: The ROC curve plotted when GMM was used for the case where the feature space consisted of $C_{1,i}^{PD1}$ and T_i. ROC curve was plotted for the results obtained in both folds of the validation data. The area under curve for both first fold and second fold is 0.946.

5.2. Supervised learning

Given the promising clustering results reported in the previous section, it was then investigated whether it was possible to directly predict build density from the aforementioned features using regression techniques. Specifically, the features such as $C_{1,i}^{PD1}$ and T_i appeared to be quite helpful in identifying categories of densities.

GP regression with Automatic Relevance Determination was used to predict the density of the specimens. In order to train the algorithm, 50% of the data (the first 31 datasets) was used and, once the optimum GP hyperparameters were estimated, the remaining 50% of the data was used to validate the algorithm. 2-fold cross validation was again performed to

Table 4: Results of GP regression with ARD

RMS error	3.65%
Length scale for no of samples	9.213×10^{-1}
Length scale for $C_{1,i}^{PD1}$	6.557×10^{3}
Length scale for $C_{1,i}^{PD2}$	1.426×10^{4}
Length scale for $C_{1,i}^{PD3}$	4.893

measure the predictive power of the algorithm outside the training set. The RMS error for each of the analyses was calculated using

$$\text{RMS of cross-validation} = \frac{\sum_{j=1}^{2}\left(\frac{1}{31}\sum_{i=1}^{31}(d_{*(i,j)} - d_{(i,j)})^2\right)^{1/2}}{2} \tag{24}$$

where $d_{*(i,j)}$ represents the predicted density of the i^{th} part in the j^{th} fold while $d_{(i,j)}$ represents the measured density of the i^{th} part in the j^{th} fold.

As reported in Table 4, the averaged RMS error was 3.65%. The predicted density is plotted against the measured density in Figure 9(a). The blue error bars represent a single standard deviation from the mean of each predicted density. An ideal predictive model that can predict the exact measured density would place all predictions over the black diagonal line. The results follow the line closely with sensible confidence bounds, indicating that the algorithm is capable of accurately predicting build density.

As explained in Section 4.2, if the j^{th} input has little predictive relevance, then the corresponding estimated lengthscale hyperparameter, L_j, will be large (effectively filtering out the j^{th} feature). Thus, referring to the lengthscale parameters reported in Table 4, it can be observed that the highest relevance was exhibited by T_i and $C_{1,i}^{PD3}$. According to the ARD results, $C_{1,i}^{PD2}$ can be discarded for GP regression since the associated lengthscale is relatively high compared to the other lengthscales. As a result, part density was again predicted without $C_{1,i}^{PD2}$ (results plotted in Figure 9(b)). The averaged RMS error in this case was 3.75%, which is relatively close to the previous RMS error 3.65%. Therefore, $C_{1,i}^{PD2}$ has very little predictive relevance which confirms the results obtained via ARD.

This study shows the potential for predicting the quality of L-PBF builds from sensor measurements, collected from three different photodiodes. We

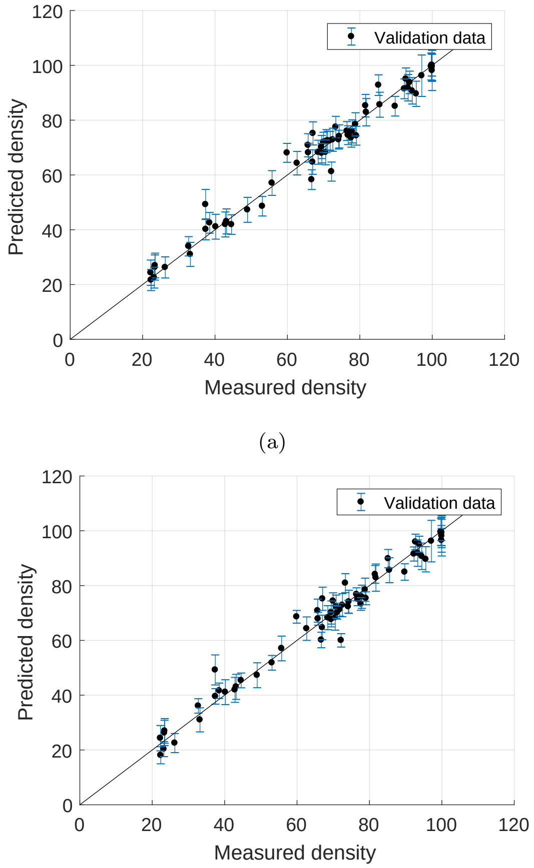

(a)

(b)

Figure 9: Measured density compared against the predicted density obtained via GP regression. The black points represent the validation data points. The blue bars on each data point represent the standard deviation of each predicted density and the black diagonal line represent the predictions of an ideal model.(a) The results obtained with all the extracted features (average RMS error was 3.65%).(b) The results obtained without $C_{1,i}^{PD2}$ (average RMS error was 3.75%).

note that build density is often required to be between 99 -100%, but the RMS error recorded was above 1%. Looking at the results produced for the six specimens with density above 99%, the RMS error was only 1.24%. As the experiment was originally designed to create specimens with a wide range of density, the number of specimens found to have density above 99% was a very small portion of the entire specimen set. Thus, we believe that by expanding the sample size and focusing the experiment on specimens with higher density the overall accuracy of the model in this region can be improved.

6. Conclusions

The absence of a robust quality control system in Additive Manufacturing introduces uncertainties regarding end-products' quality and hinders the adoption of AM technology in safety critical sectors. Most of the successful monitoring systems in the literature have focused on image-based approaches. Using only photodiode sensor measurements for online process monitoring is an open challenge that is yet to be explored in depth. Advancing this approach would be beneficial as photodiodes are cost efficient, robust, and have a relatively high sample rate.

The aim of the present research, therefore, was to investigate the feasibility of predicting part density of L-PBF builds via photodiode sensor data, obtained during the build process. Firstly, an unsupervised clustering approach was investigated, whereby L-PBF parts were separated into 2 classes depending on their density. Features, extracted from photodiode measurements utilising a Singular Value Decomposition, were used as inputs to two different unsupervised learning algorithms (K-means and a Gaussian Mixture Model). It was shown that the L-PBF builds could be clustered, depending on density, with accuracy levels of up to 93.54%.

Given the promising nature of the results realised using unsupervised approaches, Gaussian Process regression, a supervised approach, was then used to directly predict L-PBF build density. Again, these predictions were made using features extracted from photodiode measurements. The Gaussian Process was able to predict build density with an average RMS error of 3.65%. We believe that the sample size of the training data has limited the accuracy of our approach and that, by increasing the sample size and focusing the experiment on specimens with higher density, the accuracy level could be improved.

A natural progression of this work is to focus on the identification of specific anomalies (porous structures, for example) from photodiode measurements, using the results of CT scan images and X-ray radiography images.

References

[1] T. G. Spears and S. A. Gold, "In-process sensing in selective laser melting (SLM) additive manufacturing," *Integrating Materials and Manufacturing Innovation*, vol. 5, no. 1, p. 2, 2016.

[2] *Industrial strategy: building a Britain fit for the future*, Published 27 November 2017 [Accessed on 2018-06-18]. `https://www.gov.uk/government/publications/industrial-strategy-building-a-Britain-fit-for-the-future`.

[3] M. Grasso and B. M. Colosimo, "Process defects and in situ monitoring methods in metal powder bed fusion: a review," *Measurement Science and Technology*, vol. 28, no. 4, p. 044005, 2017.

[4] G. Tapia and A. Elwany, "A review on process monitoring and control in metal-based additive manufacturing," *Journal of Manufacturing Science and Engineering*, vol. 136, no. 6, p. 060801, 2014.

[5] W. J. Sames, F. List, S. Pannala, R. R. Dehoff, and S. S. Babu, "The metallurgy and processing science of metal additive manufacturing," *International Materials Reviews*, vol. 61, no. 5, pp. 315–360, 2016.

[6] J.-P. Kruth, P. Mercelis, J. Van Vaerenbergh, L. Froyen, and M. Rombouts, "Binding mechanisms in selective laser sintering and selective laser melting," *Rapid Prototyping Journal*, vol. 11, no. 1, pp. 26–36, 2005.

[7] N. Gupta, C. Weber, and S. Newsome, "Additive manufacturing: Status and opportunities," *Science and Technology Policy Institute, Washington*, 2012.

[8] M. Bisht, N. Ray, F. Verbist, and S. Coeck, "Correlation of selective laser melting-melt pool events with the tensile properties of Ti-6al-4v eli processed by laser powder bed fusion," *Additive Manufacturing*, vol. 22, pp. 302–306, 2018.

[9] I. A. Okaro, S. Jayasinghe, C. Sutcliffe, K. Black, P. Paoletti, and P. L. Green, "Automatic fault detection for laser powder-bed fusion using semi-supervised machine learning," *Additive Manufacturing*, vol. 27, pp. 42–53, 2019.

[10] D. Alberts, D. Schwarze, and G. Witt, "In situ melt pool monitoring and the correlation to part density of Inconel® 718 for quality assurance in selective laser melting," in *International Solid Freeform Fabrication Symposium, Austin, TX, USA*, pp. 1481–1494, 2017.

[11] S. Coeck, M. Bisht, J. Plas, and F. Verbist, "Prediction of lack of fusion porosity in selective laser melting based on melt pool monitoring data," *Additive Manufacturing*, vol. 25, pp. 347–356, 2019.

[12] S. Clijsters, T. Craeghs, S. Buls, K. Kempen, and J.-P. Kruth, "In situ quality control of the selective laser melting process using a high-speed, real-time melt pool monitoring system," *The International Journal of Advanced Manufacturing Technology*, vol. 75, no. 5-8, pp. 1089–1101, 2014.

[13] M. Khanzadeh, S. Chowdhury, M. Marufuzzaman, M. A. Tschopp, and L. Bian, "Porosity prediction: Supervised-learning of thermal history for direct laser deposition," *Journal of Manufacturing Systems*, vol. 47, pp. 69–82, 2018.

[14] M. Aminzadeh and T. R. Kurfess, "Online quality inspection using bayesian classification in powder-bed additive manufacturing from high-resolution visual camera images," *Journal of Intelligent Manufacturing*, vol. 30, no. 6, pp. 2505–2523, 2019.

[15] C. Gobert, E. W. Reutzel, J. Petrich, A. R. Nassar, and S. Phoha, "Application of supervised machine learning for defect detection during metallic powder bed fusion additive manufacturing using high resolution imaging.," *Additive Manufacturing*, vol. 21, pp. 517–528, 2018.

[16] T. Craeghs, S. Clijsters, E. Yasa, and J.-P. Kruth, "Online quality control of selective laser melting," in *Proceedings of the Solid Freeform Fabrication Symposium, Austin, TX*, pp. 212–226, 2011.

[17] M. Mani, S. Feng, B. Lane, A. Donmez, S. Moylan, and R. Fesperman, *Measurement science needs for real-time control of additive manufacturing powder bed fusion processes.* US Department of Commerce, National Institute of Standards and Technology, 2015.

[18] I. Yadroitsev, P. Bertrand, and I. Smurov, "Parametric analysis of the selective laser melting process," *Applied Surface Science*, vol. 253, no. 19, pp. 8064–8069, 2007.

[19] T. Kurzynowski, E. Chlebus, B. Kuźnicka, and J. Reiner, "Parameters in selective laser melting for processing metallic powders," in *High Power Laser Materials Processing: Lasers, Beam Delivery, Diagnostics, and Applications*, vol. 8239, p. 823914, International Society for Optics and Photonics, 2012.

[20] H. Gu, H. Gong, D. Pal, K. Rafi, T. Starr, and B. Stucker, "Influences of energy density on porosity and microstructure of selective laser melted 17-4ph stainless steel," in *International Solid Freeform Fabrication Symposium, Austin, TX, USA*, p. 474, 2013.

[21] Y. M. Arısoy, L. E. Criales, T. Özel, B. Lane, S. Moylan, and A. Donmez, "Influence of scan strategy and process parameters on microstructure and its optimization in additively manufactured Nickel alloy 625 via laser powder bed fusion," *The International Journal of Advanced Manufacturing Technology*, vol. 90, no. 5-8, pp. 1393–1417, 2017.

[22] G. Tapia, A. Elwany, and H. Sang, "Prediction of porosity in metal-based additive manufacturing using spatial gaussian process models," *Additive Manufacturing*, vol. 12, pp. 282–290, 2016.

[23] T. Craeghs, F. Bechmann, S. Berumen, and J.-P. Kruth, "Feedback control of layerwise laser melting using optical sensors," *Physics Procedia*, vol. 5, pp. 505–514, 2010.

[24] C. Fu and Y. Guo, "3-dimensional finite element modeling of selective laser melting Ti-6Al-4V alloy," in *International Solid Freeform Fabrication Symposium, Austin, TX, USA*, pp. 1129–1144, 2014.

[25] B. Foster, E. Reutzel, A. Nassar, B. Hall, S. Brown, and C. Dickman, "Optical, layerwise monitoring of powder bed fusion," in *Solid Freeform Fabrication Symposium, Austin, TX, Aug*, pp. 10–12, 2015.

[26] P. Lott, H. Schleifenbaum, W. Meiners, K. Wissenbach, C. Hinke, and J. Bültmann, "Design of an optical system for the in situ process monitoring of selective laser melting (SLM)," *Physics Procedia*, vol. 12, pp. 683–690, 2011.

[27] S. Berumen, F. Bechmann, S. Lindner, J.-P. Kruth, and T. Craeghs, "Quality control of laser-and powder bed-based Additive Manufacturing (AM) technologies," *Physics Procedia*, vol. 5, pp. 617–622, 2010.

[28] R. A. Horn and C. R. Johnson, "Norms for vectors and matrices," *Matrix analysis*, pp. 313–386, 1990.

[29] C. M. Bishop, *Pattern recognition and machine learning*. springer, 2006.

[30] R. Fletcher, *Practical methods of optimization*. John Wiley & Sons, 2013.